Article

Cell Chemical Biology

SIM imaging resolves endocytosis of SARS-CoV-2 spike RBD in living cells

Graphical abstract

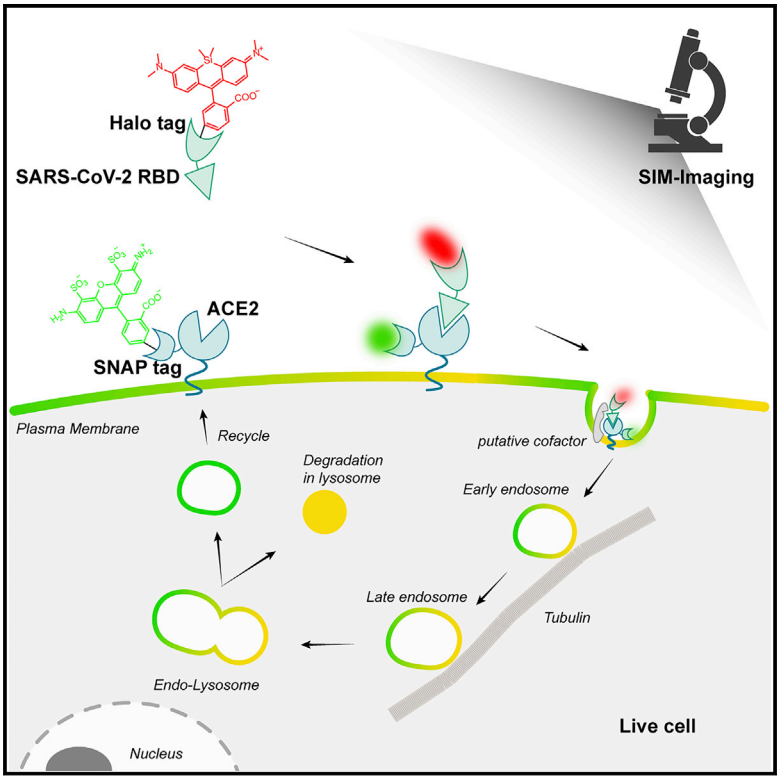

Authors

Lu Miao, Chunyu Yan, Yingzhu Chen, Wei Zhou, Xuelian Zhou, Qinglong Qiao, Zhaochao Xu

Correspondence

zcxu@dicp.ac.cn

In brief

Miao et al. genetically encoded RBD and ACE2 with Halo/SNAP tags and then labeled them with rhodamine/cyanine dyes. SIM imaging resolved endocytosis of RBD-ACE2 binding in living cells, including RBD-ACE2 recognition on the plasma membrane, cofactor-regulated membrane internalization, RAB-bearing vesicle formation and transport, RAB degradation, and downregulation of ACE2.

Highlights

- RBD endocytosis is resolved by imaging the location and ratio of ACE2/RBD fluorescence
- Exploring the initiation and influencing factors of RBD internalization
- The movement and maturation of ACE2/RBD co-localized vesicles are tracked by SIM imaging
- The RBD-ACE2 complex is taken up and degraded by lysosomes

Miao et al., 2023, Cell Chemical Biology *30*, 248–260
March 16, 2023
https://doi.org/10.1016/j.chembiol.2023.02.001

CellPress

CellPress

Cell Chemical Biology

Article

SIM imaging resolves endocytosis of SARS-CoV-2 spike RBD in living cells

Lu Miao,[1,3] Chunyu Yan,[1,2,3] Yingzhu Chen,[1] Wei Zhou,[1,2] Xuelian Zhou,[1,2] Qinglong Qiao,[1] and Zhaochao Xu[1,2,4,*]

[1]CAS Key Laboratory of Separation Science for Analytical Chemistry, Dalian Institute of Chemical Physics, Chinese Academy of Sciences, 457 Zhongshan Road, Dalian 116023, China

[2]Zhang Dayu School of Chemistry, Dalian University of Technology, Dalian 116012, China

[3]These authors contributed equally

[4]Lead contact

*Correspondence: zcxu@dicp.ac.cn

https://doi.org/10.1016/j.chembiol.2023.02.001

SUMMARY

It is urgent to understand the infection mechanism of severe acute respiratory syndrome coronavirus 2 (SARS-CoV-2) for the prevention and treatment of COVID-19. The infection of SARS-CoV-2 starts when the receptor-binding domain (RBD) of viral spike protein binds to angiotensin-converting enzyme 2 (ACE2) of the host cell, but the endocytosis details after this binding are not clear. Here, RBD and ACE2 were genetically coded and labeled with organic dyes to track RBD endocytosis in living cells. The photostable dyes enable long-term structured illumination microscopy (SIM) imaging and to quantify RBD-ACE2 binding (RAB) by the intensity ratio of RBD/ACE2 fluorescence. We resolved RAB endocytosis in living cells, including RBD-ACE2 recognition, cofactor-regulated membrane internalization, RAB-bearing vesicle formation and transport, RAB degradation, and downregulation of ACE2. The RAB was found to activate the RBD internalization. After vesicles were transported and matured within cells, RAB was finally degraded after being taken up by lysosomes. This strategy is a promising tool to understand the infection mechanism of SARS-CoV-2.

INTRODUCTION

The pandemic of COVID-19 has stimulated research on the infection mechanism of its causative virus severe acute respiratory syndrome coronavirus 2 (SARS-CoV-2) for promising therapeutic strategy. After the receptor-binding domain (RBD) of viral spike protein binds to the angiotensin-converting enzyme 2 (ACE2) of the airway epithelial cells, SARS-CoV-2 enters the cell and finally releases RNA to cause disease.[1] Therefore, the mechanism of the RBD-ACE2 binding (RAB) and subsequent entry process has become the focus of understanding viral infection.[2] RBD, S1 protein, or spike-coated pseudoviruses are generally used as alternatives to real viruses for biosafety reasons. Computer simulation and crystallography studies revealed the RAB interface.[3–7] Compared with the SARS-CoV RBD, several residue changes in the SARS-CoV-2 RBD stabilized two virus-cell binding hotspots to get 10 times higher affinity,[7] possibly explaining why SARS-CoV-2 is more harmful. The way the SARS-CoV-2 Wuhan isolate enters cells has been suggested to be diverse, including cell surface fusion or endocytosis,[8] and the current widespread Omicron strains have altered its preference to a cathepsin-dependent endosomal route of entry.[9] Through immunofluorescence imaging or reporter gene analysis of cells stimulated with target protein inhibitors, the pseudovirus-ACE2 complex was found to be internalized via clathrin-mediated endocytosis into the endolysosomes, where S2′ cleavage was performed by lysosomal cathepsin L or furin-like proteases.[10–13] The multi-stage and multi-molecular synergy characteristics of virus infecting cells are constantly proving that only research at the level of living cells can fully and truly reveal the mechanism of virus infection and thus discover more potential therapeutic targets. For example, heparin was found to synergistically help ACE2 to bind viruses on the cell membrane in living cells.[14] In another study, ACE2 cytoplasmic domain signaling was found to be unimportant for virus entry in living cells.[15] Unfortunately, so far, the entire process of SARS-CoV-2 infecting living cells has not been tracked in real time.

The binding of RBD to ACE2 was reported to be strong, dynamic, and heterogeneous, with variable dissociation constants spanning three orders of magnitude from 4.7 to 133.3 nM.[3–5] The RAB was also highly environment sensitive. For example, it has been reported that the binding free energy of RAB residues was significantly different at different temperatures.[16] This requires that modifications to RBD and ACE2 do not alter their respective activities and behaviors *in situ*. In addition, virus infection of cells is a multi-stage process, which requires spatial and temporal resolution for analytical methods.[17] Due to the dynamic, variable, and unpredictable nature of RAB and endocytosis, which simultaneously requires RBD and ACE2 to remain active *in situ*, it has been a challenge to reveal the whole process of virus infection of cells in real time.

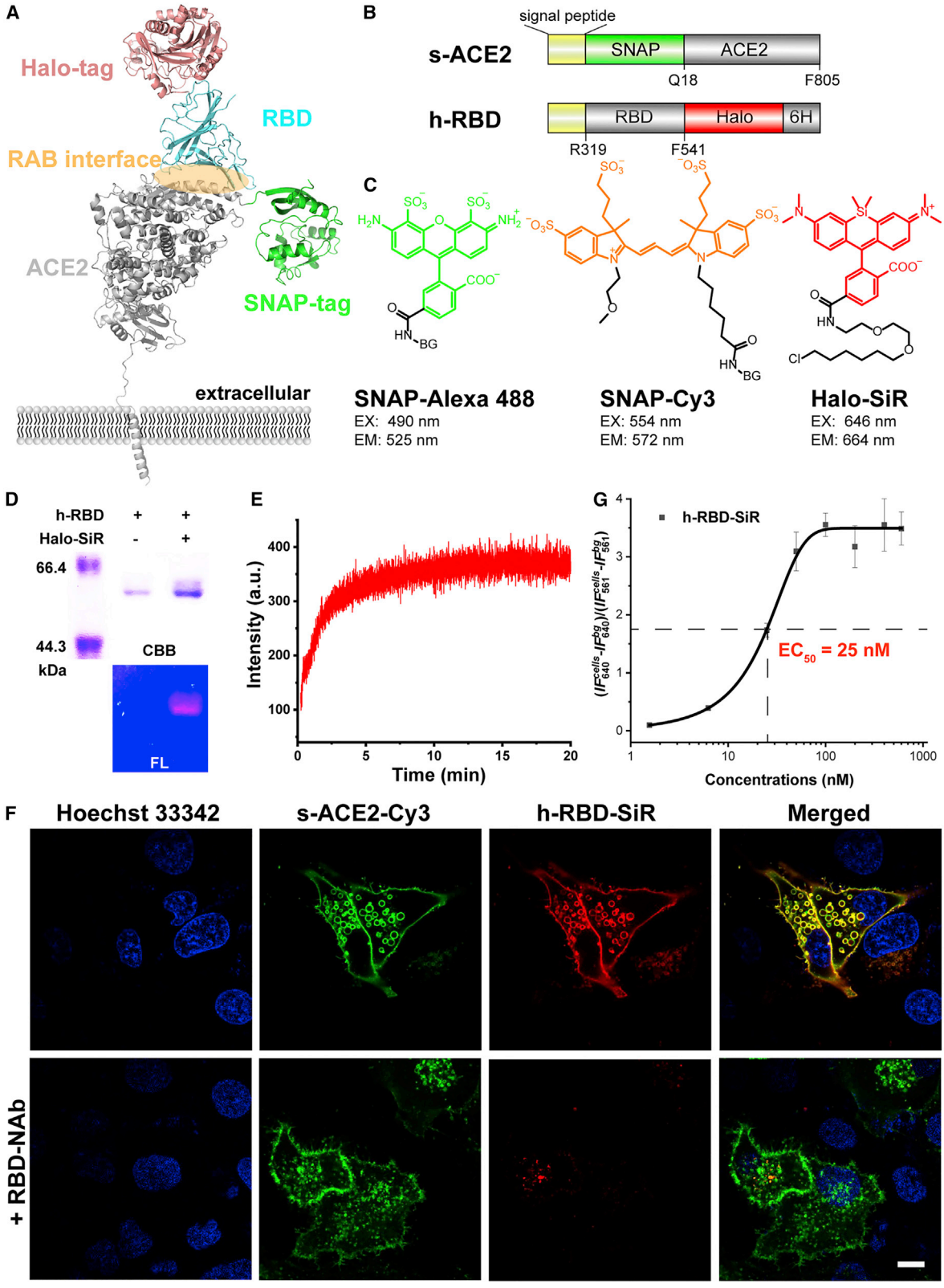

Figure 1. RAB tracking in living cells

(A) Design of fusion proteins based on RAB crystal structure (PDB: 6M17). The area with orange shadow was the RAB interface.

(B) Schematics of s-ACE2 and h-RBD constructs.

(legend continued on next page)

Structured illumination microscopy (SIM) has emerged as one of the most universally implemented optical super-resolution techniques that can surpass the optical diffraction limit, due to its mildness to fluorophores, high temporal resolution, and dynamic imaging capabilities.[18–22] The outstanding photostability and brightness of organic fluorescent dyes, as well as flexibility in choice, make them the preferred choice for super-resolution imaging.[23–28] Self-labeling strategies such as SNAP tag and Halo tag have genetically encoded components and synthetic components and combine protein site specificity with the flexibility of chemical reagents. Its combination with organic fluorescent dyes has been widely used in dynamic super-resolution fluorescence imaging of protein-protein interactions and protein-labeled subcellular structures.[29–35]

In this article, we genetically encoded the RBD and ACE2 with Halo and SNAP tags, respectively, and labeled them with rhodamine and cyanine dyes to track the RAB and endocytosis in living cells (Figure 1). Benefitting from site-specific labeling and virtually no background fluorescence, the RAB could be quantified by the intensity ratio of RBD/ACE2 fluorescence during *in situ* imaging of living cells. Notably, the long-term and multi-color SIM imaging of RAB resolved endocytosis in detail. The fate of the RBD was identified to include five consecutive stages, in the order RBD-ACE2 recognition on the plasma membrane, cofactor-regulated membrane internalization, RAB-bearing vesicle formation and transport, RAB degradation, and ACE2 recycling. Of particular importance, fluorescence signal quantification and spatiotemporal super-resolution imaging on live cells allowed us to discover that the binding of the RBD to ACE2 on the cell membrane activates the generation of vesicles responsible for loading the RBD into cells, as well as at the RBD's fate endpoint, i.e., after being degraded by lysosomes, ACE2 in vesicles responsible for transport was released into the cytoplasm. These new findings may imply undiscovered details of the mechanism of viral infection, which could potentially be used for the study of new therapeutic targets.

RESULTS

Design and organic dye labeling of RBD/ACE2 fusion protein

The design of the fusion proteins was based on the crystal structure of RAB as shown in Figure 1A (PDB: 6M17).[6] RBD S438-Q506 residues (orange shadow) interacted with ACE2 receptor, and both N- and C-terminals of the RBD were far from the interaction region. We then assigned Halo tag to the C-terminal of truncated RBD R319-F541 residues of wild-type SARS-CoV-2 spike protein and designed an RBD-Halo (h-RBD) fusion protein with molecular weight of about 59 kDa, and Halo-dyes can specifically label prepurified h-RBD proteins (Figures 1B, 1D, and S1A). The N-terminal of ACE2 was exposed on the extramembrane region in living cells.[6,36] Thus, we constructed SNAP-ACE2 (s-ACE2) by fusing SNAP tag to the N-terminal of ACE2's full sequence (residues Q18-F805) (Figure 1B). The selection of fluorescent probes needs to comprehensively consider biocompatibility, the ability of wash-free imaging, and the requirements of super-resolution imaging on optical performance.[37] The membrane-impermeable fluorescent probes were labeled with s-ACE2 and washed to remove excess extracellular ones, which could ensure the fluorescence signal selectivity of subsequent RAB tracking, because only the fluorescent probes labeled with s-ACE2 could enter cells. SNAP-Alexa 488 and SNAP-Cy3 were then selected to label s-ACE2 due to their membrane impermeability, high brightness and photostability, and access of different fluorescent channels (λ_{ex} = 488 or 561 nm) (Figure 1C). Due to its excellent brightness and photostability, Si-rhodamine has become a star fluorophore in super-resolution imaging, and its near-infrared emission (λ_{ex} = 640 nm) can also be distinguished from s-ACE2-stained colors, enabling multi-color imaging of RAB. More importantly, the Si-rhodamine (SiR) probe will convert from nonfluorescent spirolactone to fluorescent zwitterion after binding to the target protein, thus possessing fluorogenicity.[38] Halo-SiR was then selected as the fluorogenic probe for h-RBD labeling (Figures 1C and 1D). Fluorescence spectra of Halo-SiR were recorded after the addition of h-RBD from 0 to 20 min, and the results showed that the labeling of h-RBD by Halo-SiR (hereinafter referred to as h-RBD-SiR) was quickly completed within 3 min (Figure 1E). The colocalization results of both western blotting and immunofluorescence imaging proved that the specificity of the Halo protein tag to RBD protein (Figures S1A and S1B). These probes did not change their fluorescence in acid, which ensured no lysosome interference when tracking RAB in cells. Meanwhile, both SNAP and Halo dyes at 125 nM to 1 μM showed no significant toxicity to Hela and HEK293T cells after incubation for 24 h (Figures S1C–S1F).

Fluorescence imaging of the binding of h-RBD to s-ACE2 on the cell surface

Confocal fluorescence imaging was used to track the binding of h-RBD to s-ACE2 in living cells and to assess whether fusion protein modifications affected their activity (Figure 1F). We first labeled s-ACE2 with 250 nM SNAP-Cy3 (hereinafter referred to as s-ACE2-Cy3) and then added h-RBD-SiR. As expected, a colocalization imaging between s-ACE2-Cy3 and h-RBD-SiR on the cell surface was observed, while h-RBD-SiR cannot stain the cells without expressing s-ACE2 (Figure S1G). The addition of RBD neutralizing antibody (RBD-NAb) competed h-RBD from the binding complex with s-ACE2, and the red fluorescence on the cell membrane disappeared. This result verifies that the colocalization of red and green fluorescence on the cell membrane was derived from the selective binding of h-RBD to

(C) Chemical structures and maximum absorption/emission wavelengths of Halo/SNAP probes.
(D) SDS-PAGE of the fusion protein h-RBD before and after reacting with Halo-SiR. Staining under Coomassie bright blue (CBB) and UV-fluorescent light (FL), respectively.
(E) Time dependence of fluorescence intensity of Halo-SiR (2 μM) with the addition of 1 μM h-RBD.
(F) Fluorescence imaging of s-ACE2-overexpressed HeLa cells stained with Hoechst 33342, SNAP-Cy3, and h-RBD-SiR without or with the addition of RBD neutralizing antibody (RBD-NAb). λ_{ex} = 405, 561, and 640 nm, respectively. Scale bar: 10 μm.
(G) The relative activity of h-RBD to s-ACE2 in living HeLa cells. EC_{50} = 25 nM.

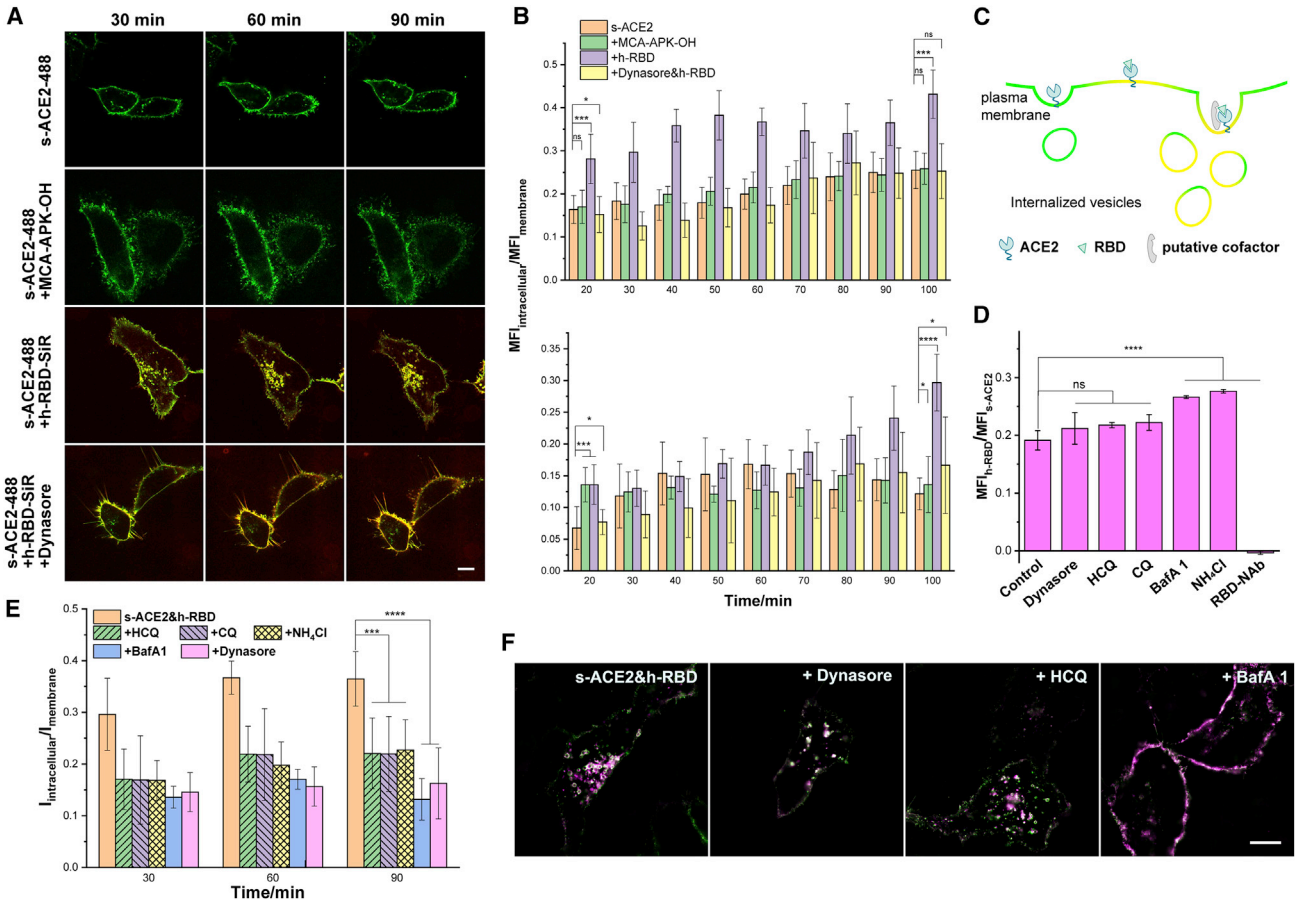

Figure 2. Extensive internalization of RBD depends on RAB and clathrin

(A) Fluorescent imaging of s-ACE2-overexpressed HeLa cells treated with SNAP-Alexa488, h-RBD-SiR, MCA-AKP-OH (100 nM), or dynasore (50 μM) at 30, 60, and 90 min, respectively. Scale bar: 10 μm.

(B) HeLa/HEK293T cell endocytosis analysis by real-time fluorescent tracking of the mean fluorescence intensity (MFI) ratio of s-ACE2-488 intracellular to that on the cell membrane.

(C) Schematic describing vesicles internalization with or without RAB.

(D) Fluorescent imaging analysis of s-ACE2&h-RBD interactions after preincubation of various inhibitors, measured by the MFI ratio between the h-RBD-SiR and s-ACE2-488 channels on the cell membrane. 40–60 cells for each test were tracked with 10× oil-dripping objective lens of living cell laser scanning confocal microscope.

(E) Fluorescent imaging analysis of h-RBD internalization after preincubation of various inhibitors, measured by the MFI ratio of s-ACE2-488 inside and on the cell membrane. Inhibitors: 50 μM dynasore, 50 μM HCQ, 50 μM CQ, 100 nM BafA1, 20 mM NH_4Cl, and 40 nM RBD-NAb. The experiments were repeated at least three times, and 7–12 cells for each test were tracked with 100× oil-dripping objective lens of living cell laser scanning confocal microscope. Statistical analysis was by one-way ANOVA (not significanct [ns] $p > 0.5$, *$p < 0.5$, **$p < 0.05$, ***$p < 0.005$, ****$p < 0.0005$).

(F) The SIM image of s-ACE2&h-RBD-based HeLa cells before and after incubation of dynasore, HCQ, and BafA1. Scale bar: 10 μm.

s-ACE2 and also demonstrates that Halo-SiR was an excellent fluorogenic probe for h-RBD. We also transiently transfected cells with ACE2-SV40-EGFP plasmid. HeLa cells expressed unmodified ACE2 on the cell surface while EGFP was simultaneously expressed in the cytoplasm (Figure S1H). The red fluorescence observed on the cell surface further supported the selective binding of h-RBD-SiR to unmodified ACE2. The activity of h-RBD and s-ACE2 was evaluated in living cells by the dependence of the intensity ratios of emission from h-RBD-SiR channel to that of s-ACE2-Cy3 on the concentration of h-RBD-SiR (Figure 1G). EC_{50} was calculated to be 25 nM, demonstrating that the RBD and ACE2 still maintain activity and have strong affinity after modification of Halo/SNAP tags, respectively.

Real-time tracking of RBD internalization to explore the initiating factors of endocytosis

For SARS-CoV-2, ACE2 is its cell membrane receptor, but how the virus is endocytosed into cells remains unclear. In our study, Figures 1F and S1I showed that there were abundant internalization vesicles containing colocalized RBD and ACE2 in the cytosol of various s-ACE2-overexpressed cells (including HEK293T, Hela, Caco-2, H1299, and Vero cells), but they were indeed absent in HeLa cells that did not overexpress s-ACE2 (Figure S1G) due to the fact that HeLa cells expressed barely endogenous ACE2 protein. Indeed, in the absence of h-RBD, we found that cells expressing s-ACE2 continuously internalized the ACE2 in the form of intracellular vesicles (in Figure 2A, first line). Here,

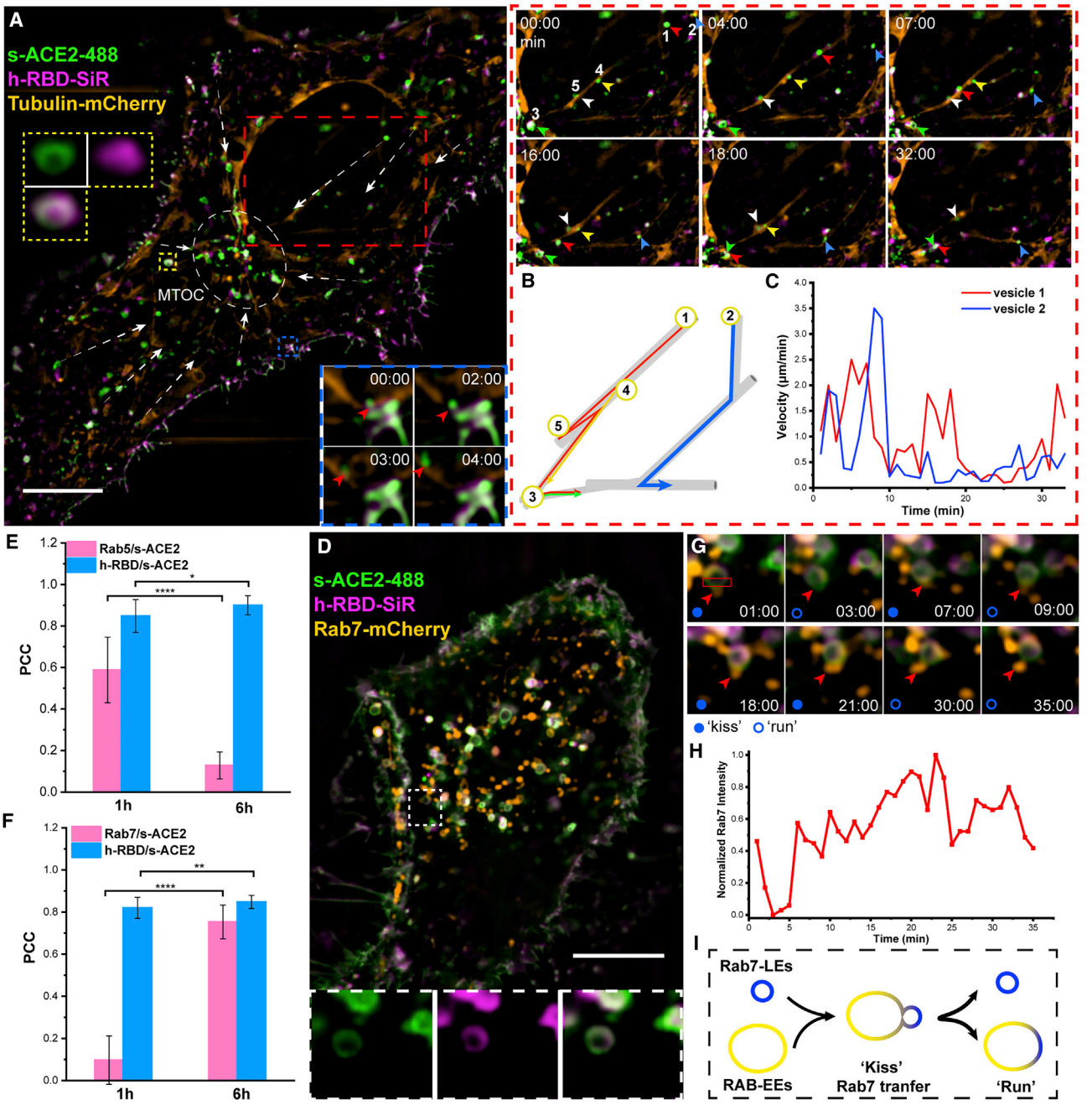

Figure 3. SIM tracking of the movement and maturation of s-ACE2-488/h-RBD-SiR colocalized vesicles

(A) The SIM image of s-ACE2 and tubulin-mCherry co-expressed HeLa cell treated with SNAP-Alexa488 and h-RBD-SiR. The formation (blue box) and the movement (red box) of the vesicles were observed by time-lapse images. The time interval between each SIM image was 1 min with a course of 33 min. Yellow box: enlarged imaging of s-ACE2-488, h-RBD-SiR, and merged channels. Scale bar: 10 μm.

(B) Illustration of the moving trajectory of red box vesicles along the microtubules.

(C) Analysis of mean velocity of the vesicles 1 and 2 shown in (B).

(D) The SIM image of s-ACE2 and Rab7-mCherry coexpressed HeLa cells treated with SNAP-Alexa 488 and h-RBD-SiR for 6 h. Scale bar: 10 μm.

(E and F) Pearson's correlation coefficient (PCC) of Rab5/Rab7/h-RBD to s-ACE2 in the SIM imaging of Figures S3A and S3B. The cells co-expressed s-ACE2&Rab5-EGFP (E) or s-ACE2&Rab7-mCherry (F). SIM imaging of living HeLa cells were obtained after coincubation of SNAP dyes and h-RBD-SiR at 1 and 6 h. The PCCs of about 300 vesicles in 6 cells were calculated using ImageJ, respectively. p values were considered significant when $p < 0.01$ and are denoted as $^{*}p < 1$, $^{**}p < 0.1$, and $^{****}p < 0.001$.

(legend continued on next page)

excessive SNAP-Alexa 488 was incubated to completely label s-ACE2 (referred to as s-ACE2-488), and these endocytic events appeared to be stable and initiated at random or spatially nonrandom sites.

In a sharp contrast, the internalization of vesicles containing s-ACE2 and h-RBD was dramatically enhanced when h-RBD was added to cells (Figures 2A, third line, and S1I; Video S1). The ratio of fluorescence intensity of s-ACE2 on the cell membrane and in the cytosol was used to quantify the degree of vesicle internalization with or without h-RBD (Figures 2B and S1J). This fluorescence intensity ratio in these cells, including HeLa, HEK293T, H1299, Vero, and Caco-2, increased significantly within 100 min after the addition of h-RBD, which meant that a large amount of s-ACE2 carried h-RBD into the cells. With the addition of dynasore, a clathrin-dependent endocytosis inhibitor, there were no s-ACE2-bearing vesicles in the cytosol (Figure 2A, fourth line), and the fluorescence intensity of s-ACE2 on the cell membrane increased. Importantly, the degree of s-ACE2 internalization was almost unchanged (Figure 2A, second line) before and after the addition of its original substrate MCA-APK(Dnp)-OH, where ACE2 can hydrolyze the peptide bond between the proline and lysine residues of peptide APK.[39]

These results suggested that ACE2-containing vesicles behaved as RBD cargo carriers during endocytosis and the RAB activated the RBD internalization, which relied on a clathrin-mediated endocytic pathway. After RBD binds to ACE2, ACE2-containing vesicles increase dramatically in cells, implying that the internalization of RAB is likely to be initiated by the aid of other factors. In this way, the initial process of the RBD entering cells can be decomposed into three stages: binding to ACE2, initiation of RAB internalization regulated by putative cofactors, and generation of internalized vesicles (Figure 2C).

Based on the ratio of fluorescence intensity of h-RBD-SiR and s-ACE2-Cy3, or ACE2 fluorescence in the cytosol and on the cell membrane, different types of inhibitors can be evaluated separately (Figures 2D and 2E). RBD-NAb blocked the RAB with the disappearance of h-RBD-SiR fluorescence, while dynasore and the endosomal acidification inhibitor chloroquine (CQ), hydroxychloroquine (HCQ), bafilomycin A1 (BafA1; V-ATPase inhibitor), and NH_4Cl cannot block the binding of h-RBD to s-ACE2 at all, and dynasore inhibited clathrin-mediated vesicles accompanied by a decrease in intracellular fluorescence intensity. Surprisingly, we found that CQ, HCQ, BafA1, and NH_4Cl displayed certain RBD endocytic inhibition if preincubating these inhibitors with cells for 30 min (Figure 2E). Among them, HCQ, CQ, and NH_4Cl inhibit endocytosis of RBD by about 40%, with an inhibiting effect that was lower than dynasore. But 100 nM BafA1 displayed an even higher inhibiting effect than that of 50 μM dynasore, where about 64% of RBD endocytosis was inhibited. SIM imaging showed that cells incubated with HCQ, dynasore, and BafA1 indeed have fewer h-RBD&s-ACE2 endocytic vesicles than those in the h-RBD-only group. In addition, the size of vesicles in cells incubated with BafA1 was significantly smaller than that in cells incubated with other drugs (Figure 2F). The antivirus activity of BafA1 was recently discovered and attributed to deactivation of TMPRSS2 and cathepsin B and L,[1,12,40] but whether the inhibition of RBD endocytosis by BafA1 discovered here for the first time is related to its antiviral property is worth further study.

The movement and maturation of s-ACE2/h-RBD colocalized vesicles tracked by SIM imaging

Figure 3 and Videos S2 and S3 showed the dynamic SIM imaging of RAB at different times after entering the cell (Figure 3A/Video S2: 1 h after adding h-RBD; Figure 3E/Video S3: 6 h after adding h-RBD). Small-sized vesicles were first generated at the cell membrane (blue box in Figure 3A), then moved along the microtubules from the outside of the cell to the nucleus, and then spread out after being concentrated in the microtubule organizing center (MTOC). According to the statistics, during this period, about 23.6% of the intracellular h-RBD/s-ACE2 vesicles have located near the MTOC and had a small degree of disordered motion, while about 31.5% of the h-RBD/s-ACE2 vesicles had a tendency of large motion toward the MTOC (white dotted line in Figure 3A and Video S2). No significant interaction was found between RAB and actin (Video S4). Figure S2A displays that the vesicle in dotted box 1 increased in diameter from 1.45 to 2 μm within 20 min, during which time it undergoes multiple fusion processes. The velocities of some vesicle movements were fast (up to 3.5 μm/min) until reaching the MTOC and slowed down (0.2–0.5 μm/min) significantly after diffusing outward from the MTOC (Figure 3C). Also, we captured the reciprocating motion of vesicles on microtubules, as well as orbital transitions across multiple microtubules. In the red box of Figure 3A, vesicle 1 moved from one microtubule to another and then switched to the third microtubule after fusion with vesicle 3 (more details in Video S2 and Figures S2B–S2D). At the same time, vesicle 2 traveled rapidly along the other three microtubules. A particularly interesting process was also found during the movement of vesicle 1. Along the same microtubule, vesicle 1 passed by vesicle 4, contacted with vesicle 5 further away, and then returned to vesicle 4. In the end, it did not fuse with vesicles 4 and 5 but continued to move in the direction of MTOC after leaving these two vesicles. Simulated trajectories of these vesicles are shown in Figure 3B.

After 6 h of h-RBD addition, large-sized vesicles mainly existed in the cells, and their positions were relatively stable (Figure 3D). In addition, to track the vesicular maturation process, we co-transfected cells with Rab5-EGFP and Rab7-mCherry, respectively. Rab5 and Rab7 are the best-characterized Rab proteins in the endocytic process. Rab5 is mainly associated with early endosomes (EEs), and Rab7 defines late endosomes (LEs).[41] Here, Pearson's correlation coefficient (PCC) was used to evaluate the colocalization of Rab5 or Rab7 and s-ACE2-containing vesicles (Figures 3E, 3F, S3A, and S3B). From 1 to 6 h after incubating h-RBD, PCC between s-ACE2 and Rab5 decreased from 0.59 to 0.13 and PCC between s-ACE2 and Rab7 increased from 0.10 to 0.82. This meant that the vesicles were EEs at 1 h and

(G) Time-lapse SIM images of white boxed regions in (D). The time interval between each SIM image was 1 min with a course of 35 min.
(H) Normalized Rab7 intensity of red box region of the vesicle in (G).
(I) Illustration of the Rab7 transferring from LEs to RAB-based EEs. Excitation: 488, 561, and 640 nm. Scale bar: 10 μm.
See also Figures S2 and S3.

matured into LEs after 6 h. During this period, the colocation of h-RBD and s-ACE2 remained constant (PCC: 0.8–0.9). This relatively low PCC of h-RBD/s-ACE2 colocation was due to the fact that only part of the s-ACE2 in the vesicle was bound to h-RBD (Figure 2C), which was also confirmed by SIM imaging. Further study found that incubation with HCQ, BafA1, and dynasore did not affect the transformation of the h-RBD&s-ACE2 endocytotic vesicles from early to late endocytosomes since 80% of endocytotic vesicles were colocalized with Rab5 after 1 h incubation, while after incubation for 10 h, they were colocalized with Rab7 (Figure S3C).

From the fluorescence channel imaging of randomly selected vesicles in Figures 3A (yellow box) and 3D (white box), it can be seen that SIM imaging can clearly distinguish the membrane structure of vesicles and the distribution of s-ACE2 and h-RBD, where s-ACE2 fills the entire membrane area, while h-RBD is only distributed in part of the membrane area. This also proved once again that ACE2-containing vesicles behaved as RBD cargo carriers during endocytosis. Furthermore, the dynamic process of Rab7 transferring to RAB-containing vesicles to form LEs was captured by time-lapse SIM images (Figures 3G and 3H, and more details in Video S3 and Figure S3D). Vesicles briefly contacted LEs through multiple ''kiss-and-run'' fusions, and the fluorescence of Rab7-mCherry on vesicles gradually increased (Figure 3I).

SIM imaging revealed the destinations of RBD and ACE2 proteins

SIM imaging revealed how RBD-containing LEs were degraded by lysosomes and the destinations of both RBD and ACE2 proteins (Figures 4 and S4; Video S5). The dye Lyso561 was used to stain the lysosomal lumen, while LAMP1-mCherry was used for the lysosomal membrane. At 2 h, the vesicles belonged to EEs, and there was almost no spatial contact with the lysosomes at this time, and the PCC value of Lyso561 to s-ACE2-488 was only 0.02 (Figures 4A, 4B, and S4A). SIM imaging can clearly distinguish EEs from lysosomes and the distribution of s-ACE2 and h-RBD in selected vesicles 1–5 through the intensities of fluorescence channels at different spatial locations (Figure 4A). Matured vesicles fused with lysosomes for gradual acidification. At 10 h (Figure 4A), the intracellular vesicles and lysosomes were almost completely fused, the PCC value of Lyso561 to s-ACE2-488 increased to 0.54, and the size of the vesicles increased significantly. The fluorescence intensity of Lyso561 in vesicles 2–4 of Figure 4A significantly increased, indicating that the interior of the vesicles was full of acidity. More significantly, the intracellular LEs were found to differentiate into two categories at 10 h, and the ratio of h-RBD and s-ACE2 fluorescence intensities in the vesicles changed regularly compared with EEs: one group of vesicles was h-RBD and s-ACE2 colocated on the vesicle membrane, and the statistical results showed that the ratio of h-RBD to s-ACE2 ($\sim$0.79) was lower than that of EEs ($\sim$0.95; Figure 4C); meanwhile, the h-RBD and s-ACE2 of the other vesicles were colocated in the interior of the vesicles with a significant increase of the h-RBD to s-ACE2 ratio ($\sim$1.25; Figure 4C). As we explained earlier, the intensity ratio of h-RBD and s-ACE2 indicated the degree of s-ACE2 saturation in the vesicles. The initially generated vesicles and EEs contained more s-ACE2 than h-RBD so that the vesicles contained both RAB complexes and free ACE2. So, a decrease in the intensity ratio of h-RBD to s-ACE2 means a decrease in the RAB complex's content and an increase in the free ACE2 content in the vesicles. Conversely, an increase in the intensity ratio of h-RBD to s-ACE2 implies an increase in the RAB complex's content in vesicles while a decrease in free ACE2 content.

At 17 h (Figure 4A), the size of the vesicles was significantly reduced, and vesicles with comparable h-RBD and s-ACE2 contents (such as vesicle 4) and vesicles containing only s-ACE2 (such as vesicle 5) appeared. In these vesicles with comparable contents of h-RBD and s-ACE2, the fluorescence signals of h-RBD, s-ACE2, and lysosome completely overlapped spatially. Further, by labeling the lysosomal membrane protein LAMP1, it was proved that h-RBD and s-ACE2 had indeed entered the lumen of the lysosome at 17 h (Figure 4D), indicating the degradation of RAB. The *in vitro* experiments indicated that the fluorescence of Halo-SiR remained almost constant after the degradation of Halo protein by trypsin, where SDS-PAGE analysis confirmed that Halo protein could be degraded by trypsin (Figures S4B and S4C). Western blotting of Figures 4E and 4F demonstrated that after incubation of h-RBD for 20 h, intracellular h-RBD and s-ACE2 were indeed partially degraded, and dynasore could inhibit protein degradation. This result is consistent with previous experiments. In addition, we monitored the fluorescence changes of s-ACE2 on the cell membrane of specific cells before and after incubation of h-RBD and found that the content of s-ACE2 on the cell membrane was significantly reduced after incubation of h-RBD (Figure 4G). It demonstrated that the degradation of s-ACE2 can lead to the reduction of ACE2 content in the cell membrane, which may be one of the causes of some complications (such as lung injury, etc.) during viral infection.

The number of lysosomes with RAB degradants accounted for 60% of the total lysosome. Importantly, after incubation with 100 nM BafA1, the fluorescence of RAB in lysosome was hardly observed, in that a number of them decreased to an average of 3% (Figures S4D and S4E), demonstrating the intracellular inhibitory effect of BafA1 on viral infection. BafA1 was reported to inhibit lysosomal acidification by inactivating v-ATPase. The inhibition of the protein degradation in this article resulted from the inactivation of lysosomal hydrolases in a nonacidic environment. In addition, very few lysosomes containing only h-RBD degradants were captured (Figure S4F), indicating that the RAB complex or RBD only could be acquired and degraded by lysosomes.

The above results suggest the following RAB complex degradation mechanism (Figure 4H). The lysosome selectively fuses with the RAB complex's region in the vesicle, and then the free ACE2 region in the vesicle is cleaved to form a new ACE2-only vesicle that is redistributed, and the RAB complex's region is fused with the lysosome to be degraded. In 3D SIM imaging (Figure 4I; Video S5), we did find that lysosomes were only fused to the RAB region (indicated by white arrows for ELs) and also found the coexistence of vesicles of different stages and different structures, including EEs, LEs, lysosome enzyme-encapsulated RAB (red arrow), and vesicles containing only ACE2 (blue arrow for RVs). This also proved the rationality of our proposed RAB complex's degradation mechanism. SIM imaging also demonstrated that SARS-CoV-2 RBD endocytosis and degradation was a highly dynamic and heterogeneous process.

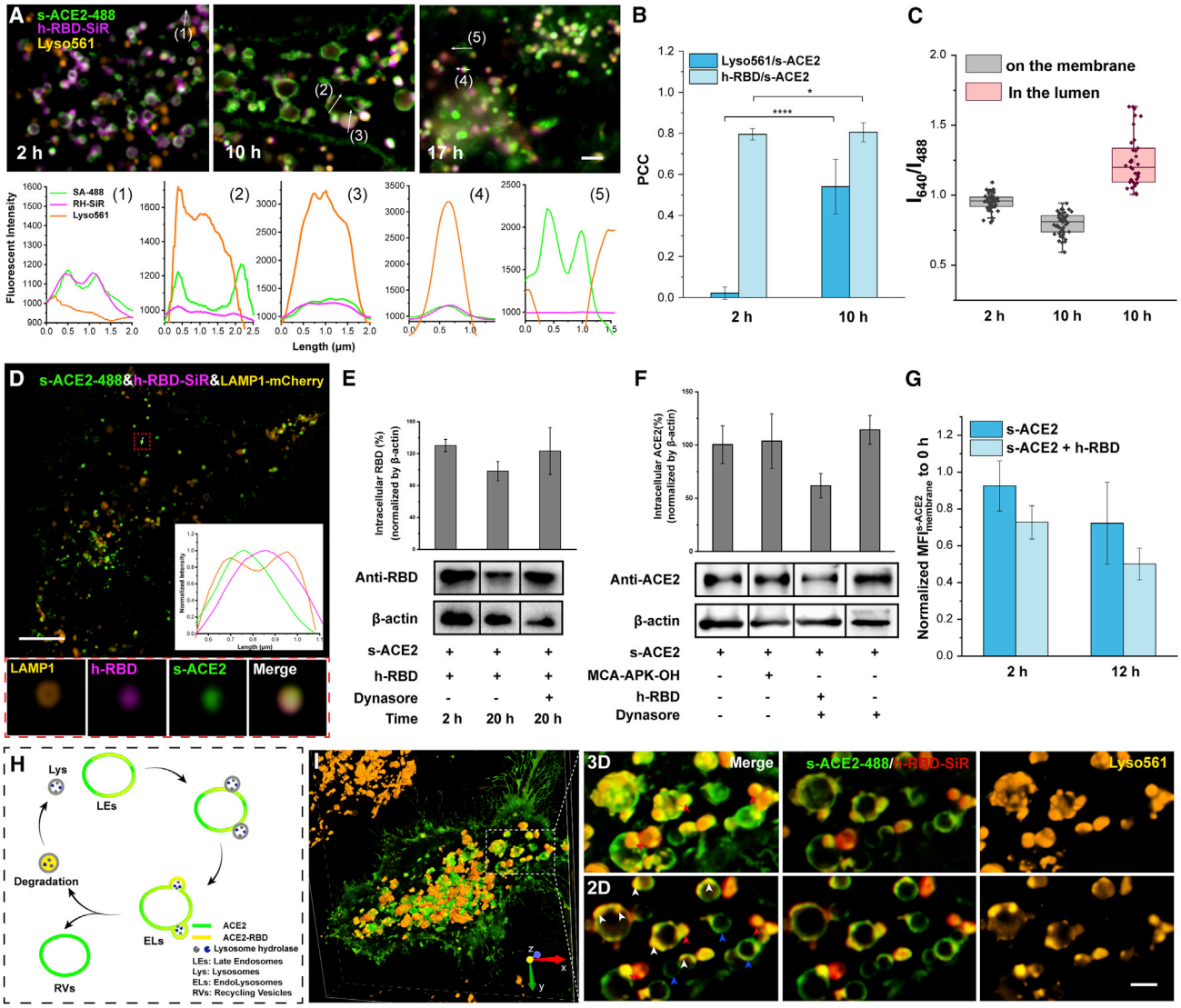

Figure 4. Degradation of s-ACE2 and h-RBD

(A) SIM imaging of live HeLa cells incubated with 25 nM h-RBD-SiR for 2, 10, and 17 h, respectively. The fluorescence intensities of s-ACE2-488 (green), h-RBD-SiR (purple), and Lyso561 (orange) across vesicles 1–5 are shown below the images. See also Figure S4A. Scale bar: 2 μm.

(B) PCC of s-ACE2&h-RBD and s-ACE2&Lyso561 colocalization. The PCC of about 300 vesicles in 6 cells were calculated at each time point, and p values were considered significant when $p < 0.01$ and are denoted as *$p < 1$ and ****$p < 0.001$.

(C) The h-RBD-SiR/s-ACE2-488 fluorescence ratios of vesicles in cells cultured after 2 and 10 h.

(D) SIM imaging of living HeLa cells co-expressing s-ACE2 and LAMP1-mCherry. Red box was the enlarged image from different channels. Inset: normalized fluorescence intensity of s-ACE2-488 (green), h-RBD-SiR (purple), and LAMP1-mCherry (orange) along the white arrow. Scale bar: 10 μm.

(E) Total h-RBD levels in HEK293T cells and supernatant after treatment with h-RBD for 2 and 20 h.

(F) Intracellular s-ACE2 levels in HEK293T cells treated with or without h-RBD, dynasore, and MCA-APK-OH for 20 h.

(G) Normalized fluorescence intensity of s-ACE2 on the same cell membrane before and after incubation of h-RBD.

(H) Illustration of s-ACE2 and h-RBD degradation or recycling. The h-RBD&s-ACE2 complex and s-ACE2 were not uniformly distributed in LEs. Lysosomes selectively acquired and degraded the h-RBD&s-ACE2 complex from LEs through kiss-and-run fusion event, where LEs formed a contact site with lysosomes ("kiss") transferring the s-ACE2&h-RBD complex with ensuing dissociation ("run").

(I) 3D-SIM and enlarged 2D/3D imaging of live HeLa cell incubated with 25 nM h-RBD-SiR for 10 h. Scale bar: 2 μm.

As a part of the spike protein, the endocytosis process of RBD protein cannot represent the complete infection process of full spike protein or the virus itself. We therefore further expressed GFP Gamillus (mGam)-labeled spike-ectodomain trimer of SARS-CoV-2 (referred to as spike-T-mGam) and imaged its endocytosis with SIM. Here, mGam is an acid-tolerant GFP that may enable fluorescent tracking when spike-T-mGam is taken up into acidic cellular organelles. We found that spike-T-mGam was first bound to s-ACE2 proteins on the cell surface and then endocytosed into cells as vesicles (Figure S5A). Compared with cells without spike-T-mGam, the degree of s-ACE2 internalization was increased (Figure S5B), and after

6 h incubation, 80% of the spike-T-mGam endocytotic vesicles were colocated with Rab7 to form LEs (Figure S5C). Furthermore, after incubation for 20 h, it was observed that the endocytic vesicles changed from the previous spike-T-mGam&s-ACE2-Cy3 colocated on the vesicle membrane to the inside of the vesicles (Figure S5A), indicating the degradation of spike-T-mGam. These experimental phenomena were consistent with the endocytosis and degradation of RBD described above, indicating the similar endocytosis process between the spike protein and RBD.

DISCUSSION

Live-cell tracking of the SARS-CoV-2 RBD and ACE2 interaction and subsequent entry process contributes to understanding the mechanism of viral infection. Here, we labeled the RBD of wild-type SARS-CoV-2 spike protein and ACE2 proteins with organic dyes by genetically encoded self-labeling protein tag, and the whole process of RBD endocytosis, including RBD-ACE2 recognition, internalization, RAB-bearing vesicle formation and transport, RAB degradation, and downregulation of ACE2 were resolved by tracking the location and ratio of RBD/ACE2 fluorescence in real time. The accurate quantification of RBD and ACE2 benefited from the site-specific, photostability organic dye fluorescence labeling of protein. After the dye is labeled to the protein, it is carried into the cell along with the internalization of the protein, avoiding the influence of background light. In particular, the dyes were acid insensitive, and the degradation of proteins did not affect the fluorescence properties of the dyes (Figures S1C, S1D, S4B, and S4C). Meanwhile, the dyes showed little toxicity at concentrations of 125 nM to 1 μM for both HeLa and 293T cells after incubation for 24 h (Figures S1E and S1F). Therefore, they can be used for long-term incubation and imaging of tissues and organs, including lung organoids. RBD-ACE2 recognition on the plasma membrane was first observed, and RBD/ACE2 inhibitors can block RAB by imaging the ratiometric of RBD/ACE2 fluorescence on the plasma membrane (Figure 3D).

Endosomal entry mechanisms provide many advantages to the viruses, allowing them to spread efficiently while evading host immune surveillance.[42] Although the SARS-CoV-2 Wuhan isolate has been reported to enter cells through a variety of pathways, including TMPRSS2-dependent cell surface membrane fusion and acidic endosomal protease-dependent endocytic pathways,[8] it has recently been demonstrated that the Omicron strain of SARS-CoV-2 is more likely to enter cells by the TMPRSS2-independent endocytic pathway,[9] which displays the importance of studying the endocytosis mechanism of the virus. There is a lot of debate about whether virus molecules are an essential component for the initiation of an endocytic event or whether they are more passive passengers that can be recruited after the initiation, and of course, there may be other mechanisms.[37] In this article, we explored the endocytic initiation of SARS-CoV-2 by tracking the degree of binding and internalization of the RBD with ACE2 in real time. ACE2 is a pivotal component of the renin-angiotensin system, promoting the conversion of angiotensin II (Ang-II) to Ang-1–7. In the cells, which lack an endogenous Ang-II type 1 receptor, Ang-II failed to promote ACE2 internalization.[43,44] This is consistent with our results: the degree of s-ACE2 internalization was almost unchanged before and after the addition of its original substrate, MCA-APK(Dnp)-OH. In contrast, by tracking the fluorescence ratio of ACE2 in the cytosol and on cell membranes before and after adding the RBD, we have demonstrated that in addition to endocytosis caused by ACE2 itself, RAB was able to initiate endocytosis of cells, making the RBD as a cargo molecule easier to be internalized into cells within 20 min (Figures 2A and 2B).

The initiation of endocytosis may be caused by multiple factors. Firstly, the RBD requires stable binding with ACE2, and studies have shown that this binding requires the assistance of cofactors such as heparin sulfate, AXL, and neuropilin-1 on the cell surface.[14,45,46] After the binding of the RBD and ACE2, endocytic capsid proteins represented by clathrin start to assemble on the inner leaflet of the plasma membrane. It promotes the film to bend and eventually forms clathrin-coated endocytic vesicles.[13] However, the origin of this clathrin pathway initiation signal remains unclear. In general, once the ligand binds to the extracellular domain of cell-surface receptors, a signal is transmitted to the intracellular domain and initiates the entry process.[8] But recent research shows that the initiation of RAB endocytosis is not affected by ACE2 cytoplasmic domain signaling.[15] Therefore, other known or unknown putative cofactors must play a key role in the initiation of RAB endocytosis (Figure 2C), such as heparin sulfate, neuropilin-1, etc. The role of these cofactors remains to be explored.

In addition, some external factors can inhibit the endocytosis of RAB. We found that HCQ and CQ inhibit viral entry prior to inhibiting cathepsin-L. This is consistent with recent findings that HCQ could block SARS-CoV-2 entry into the endocytic pathway of the cells by directly perturbing clustering of the ACE2 receptor with both endocytic lipids and PIP2 clusters,[47] and CQ is known for its efficacy in blocking the clathrin-mediated endocytosis of nanoparticles.[48] Surprisingly, BafA1 as a specific inhibitor of V-ATPase displayed a stronger inhibitory effect (64%; Figure 2E) on the internalization of RBD protein. BafA1 has been reported to inhibit receptor-mediated endocytosis of asialoglycoproteins in isolated rat hepatocytes,[49] but its strong inhibition of RAB-mediated endocytosis was first reported. Further investigation of BafA1 and its analogs as potential therapeutic agents for COVID-19 is warranted.

Multi-color SIM super-resolution imaging captured the complex and precise movements of the internalized colocalization vesicles of the RBD and ACE2 in living cells, including the fusion between vesicles (Figure S2A), vesicles' movement along microtubules (Figures 3A–3C), and the substance-exchange process from EEs to LEs (Figures 3D–3G). In addition, the vesicles formed after the internalization of the RBD showed uneven distribution of the RBD and ACE2 on the vesicle membrane, as shown as the randomly selected vesicles in Figures 3A (yellow box) and 3D (white box). This is due to the fact that the additional amount of h-RBD-SIR (25 nM) is less than the concentration of h-RBD-SIR required (>100 nM, Figure 1G) for s-ACE2 to be saturated by h-RBD. Thus, the vesicles contained both RAB complexes and free ACE2.

We further resolved the process of RBD and ACE2 arriving at the final destination through the change of h-RBD-SiR/s-ACE2-488 fluorescence ratio on or inside the vesicle membrane, where the RAB complex was degraded by lysosomes and the

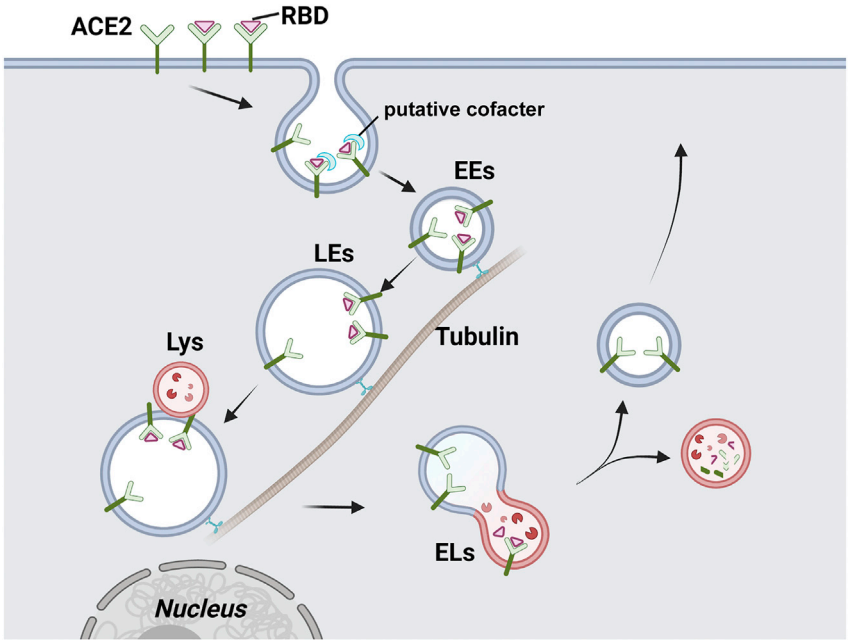

Figure 5. A proposed endocytic pathway of SARS-CoV-2 spike RBD

internalization and clathrin-dominated endocytosis, where ACE2-containing vesicles behave as RBD cargo carriers. RAB-containing internalized vesicles move along microtubules from near the cell membrane to MTOC, during which time they gradually transform into EEs and LEs. LEs and lysosomes sort the cargo by kiss-and-run events, where the RBD-ACE2 complex is more easily ingested and degraded by lysosomes, and the RBD-unbound ACE2 is reliberated into the cytoplasm and may circulate back to the cell membrane.

remaining RBD-unbound ACE2 protein maybe recycled (Figure 4), indicating ACE2-containing vesicles behavior as RBD cargo carriers during endocytosis. The mechanism of interaction between lysosomes and late endocytosomes (Figure 4E) is supported by reported studies,[50] where lysosomal fission, including vesiculation, tubulation, and kiss-and-run events occur in order to maintain steady-state levels of lysosome number and size.[51,52] Kiss-and-run events between lysosomes and endocytosomes often involve the exchange of their content despite being separate vesicles.[53] Our result demonstrated that infected viral RBDs, and possibly other capsid proteins, are eventually captured and degraded by lysosomes, even as the viral RNA is driving formation of new virus that egresses from lysosomes.[54]

As reported, the reduction of ACE2 protein level leads to a variety of diseases, such as lung injury, hypertension, and abnormal coagulation. In this article, we observed the gradual internalization of ACE2 after interaction with the RBD. Although some ACE2 may circulate back to the cell membrane (Figure 4A), the fluorescence of ACE2 on the cell membrane gradually decreases after binding with the RBD (Figure 4G), proving that the RBD has the ability to occupy and downregulate the ACE2 protein. SARS-CoV-2 infection causes partial or total loss of ACE2 function on the cell surface with the consequent accumulation of Ang-II and reduction in Ang-1–7 levels.[55] It appears to be strictly implicated in the development of severe forms of COVID-19.[56,57] ACE2 bound to the RBD was selectively degraded by lysosomes, which is one of the main reasons for ACE2 downregulation, and Ang receptor type 1 (AT1R), the bradykinin 2 receptor (B2R), and dynasore appear to modulate the downregulation of ACE2 induced by a SARS-CoV-2 surface protein.[58]

Based on the above results, we propose the following pathway of SARS-CoV-2 RBD endocytosis (Figure 5). After the RBD recognizes ACE2, the RAB actives the cofactor-regulated RAB

Limitations of the study

Some limitations should be noted. As reported, virus entry occurs through either endocytosis or fusion on the cell surface.[2] Unfortunately, it was still unable to track the events of virus-host membrane fusion and viral genome release process. However, our results demonstrate the powerful applicability of our system for the resolution of precise intracellular dynamic during SARS-COV-2 entry, including cell uptake, transport, and metabolism. In addition, as a part of virus, the endocytosis process of the RBD or even full spike protein cannot represent the complete infection process of the virus itself. Recently, we have also been trying to label small molecular dyes to four structural proteins (membrane [M], nucleoprotein [N], envelope [E], and spike protein) of SARS-CoV-2 by Halo/SNAP protein labeling methods and to assemble them into virus particles,[59] hoping to track the virus particle endocytosis process in super-resolution in real time.

SIGNIFICANCE

We have developed a live-cell visualization strategy to resolve endocytosis of the SARS-CoV-2 RBD by fusing SNAP/Halo protein tags to the RBD and ACE2. With the help of the diffraction-limited spatial resolution and the excellent dynamic imaging performance of SIM, the details of different stages of SARS-CoV-2 RBD endocytosis were first discovered. First, the binding of RBD to ACE2 initiated the internalization process, ACE2-rich vesicles were formed to transport RBD. And then RBD/ACE2 vesicles moved rapidly along the microtubule, during which the vesicles contacted, fused, exchanged substance, and transfered between different microtubules. Finally, RBD and ACE2 were taken up and degraded by lysosomes, and the free ACE2 in vesicles may be released into the cytoplasm for reuse. The degradation of the RBD-ACE2 complex predicts the downregulation of ACE2 on the cell membrane, which appears to be strictly implicated in the development of severe forms of COVID-19. The discovery of these processes has

enlightenment on the pathogenic mechanism of COVID-19 and the development of antiviral drugs, but the molecular mechanism remains to be further analyzed.

STAR★METHODS

Detailed methods are provided in the online version of this paper and include the following:

- KEY RESOURCES TABLE
- RESOURCE AVAILABILITY
  - Lead contact
  - Materials availability
  - Data and code availability
- EXPERIMENTAL MODEL AND SUBJECT DETAILS
  - Cell lines
- METHOD DETAILS
  - Fusion protein expression and purification
  - Probe synthesis
  - SDS-PAGE/Western Blot analysis
  - Live-cell imaging of RBD-ACE2 interaction
  - Live-cell tracking of h-RBD internalization
  - Live-cell evaluation of inhibitors
  - SIM dynamics imaging: transport and maturation of h-RBD&s-ACE2 vesicles
  - SIM imaging to resolve the destinations of both h-RBD and s-ACE2
- QUANTIFICATION AND STATISTICAL ANALYSIS

SUPPLEMENTAL INFORMATION

Supplemental information can be found online at https://doi.org/10.1016/j.chembiol.2023.02.001.

ACKNOWLEDGMENTS

This work is supported by the National Natural Science Foundation of China (22225806, 22078314, and 22278394) and the Dalian Institute of Chemical Physics (DICPI202227, DICPI202142).

AUTHOR CONTRIBUTIONS

Concepts were conceived by Z.X. and L.M.; L.M. designed the experiments and analyzed the data; C.Y., X.Z., and L.M. performed live-cell experiments; W.Z. and Q.Q. performed compound synthesis; L.M. and Z.X. wrote the manuscript.

DECLARATION OF INTERESTS

The authors declare no competing interests.

Received: July 15, 2022
Revised: January 5, 2023
Accepted: February 3, 2023
Published: March 7, 2023

REFERENCES

1. Yeung, M.L., Teng, J.L.L., Jia, L., Zhang, C., Huang, C., Cai, J.P., Zhou, R., Chan, K.H., Zhao, H., Zhu, L., et al. (2021). Soluble ACE2-mediated cell entry of SARS-CoV-2 via interaction with proteins related to the renin-angiotensin system. Cell *184*, 2212–2228.e12. https://doi.org/10.1016/j.cell.2021.02.053.
2. Jackson, C.B., Farzan, M., Chen, B., and Choe, H. (2022). Mechanisms of SARS-CoV-2 entry into cells. Nat. Rev. Mol. Cell Biol. *23*, 3–20. https://doi.org/10.1038/s41580-021-00418-x.
3. Shang, J., Ye, G., Shi, K., Wan, Y., Luo, C., Aihara, H., Geng, Q., Auerbach, A., and Li, F. (2020). Structural basis of receptor recognition by SARS-CoV-2. Nature *581*, 221–224. https://doi.org/10.1038/s41586-020-2179-y.
4. Lan, J., Ge, J., Yu, J., Shan, S., Zhou, H., Fan, S., Zhang, Q., Shi, X., Wang, Q., Zhang, L., et al. (2020). Structure of the SARS-CoV-2 spike receptor-binding domain bound to the ACE2 receptor. Nature *581*, 215–220. https://doi.org/10.1038/s41586-020-2180-5.
5. Wang, Q., Zhang, Y., Wu, L., Niu, S., Song, C., Zhang, Z., Lu, G., Qiao, C., Hu, Y., Yuen, K.Y., et al. (2020). Structural and functional basis of SARS-CoV-2 entry by using human ACE2. Cell *181*, 894–904.e9. https://doi.org/10.1016/j.cell.2020.03.045.
6. Yan, R., Zhang, Y., Li, Y., Xia, L., Guo, Y., and Zhou, Q. (2020). Structural basis for the recognition of SARS-CoV-2 by full-length human ACE2. Science *367*, 1444–1448. https://doi.org/10.1126/science.abb2762.
7. Wrapp, D., Wang, N., Corbett, K.S., Goldsmith, J.A., Hsieh, C.-L., Abiona, O., Graham, B.S., and McLellan, J.S. (2020). Cryo-EM structure of the 2019-nCoV spike in the prefusion conformation. Science *367*, 1260–1263. https://doi.org/10.1126/science.abb2507.
8. Grove, J., and Marsh, M. (2011). The cell biology of receptor-mediated virus entry. J. Cell Biol. *195*, 1071–1082. https://doi.org/10.1083/jcb.201108131.
9. Meng, B., Abdullahi, A., Ferreira, I.A.T.M., Goonawardane, N., Saito, A., Kimura, I., Yamasoba, D., Gerber, P.P., Fatihi, S., Rathore, S., et al. (2022). Altered TMPRSS2 usage by SARS-CoV-2 Omicron impacts infectivity and fusogenicity. Nature *603*, 706–714. https://doi.org/10.1038/s41586-022-04474-x.
10. Shang, J., Wan, Y., Luo, C., Ye, G., Geng, Q., Auerbach, A., and Li, F. (2020). Cell entry mechanisms of SARS-CoV-2. Proc. Natl. Acad. Sci. USA *117*, 11727–11734. https://doi.org/10.1073/pnas.2003138117.
11. Prabhakara, C., Godbole, R., Sil, P., Jahnavi, S., Gulzar, S.E.J., van Zanten, T.S., Sheth, D., Subhash, N., Chandra, A., Shivaraj, A., et al. (2021). Strategies to target SARS-CoV-2 entry and infection using dual mechanisms of inhibition by acidification inhibitors. PLoS Pathog. *17*, e1009706. https://doi.org/10.1371/journal.ppat.1009706.
12. Ou, X., Liu, Y., Lei, X., Li, P., Mi, D., Ren, L., Guo, L., Guo, R., Chen, T., Hu, J., et al. (2020). Characterization of spike glycoprotein of SARS-CoV-2 on virus entry and its immune cross-reactivity with SARS-CoV. Nat. Commun. *11*, 1620. https://doi.org/10.1038/s41467-020-15562-9.
13. Bayati, A., Kumar, R., Francis, V., and McPherson, P.S. (2021). SARS-CoV-2 infects cells after viral entry via clathrin-mediated endocytosis. J. Biol. Chem. *296*, 100306. https://doi.org/10.1016/j.jbc.2021.100306.
14. Clausen, T.M., Sandoval, D.R., Spliid, C.B., Pihl, J., Perrett, H.R., Painter, C.D., Narayanan, A., Majowicz, S.A., Kwong, E.M., McVicar, R.N., et al. (2020). SARS-CoV-2 infection depends on cellular heparan sulfate and ACE2. Cell *183*, 1043–1057.e15. https://doi.org/10.1016/j.cell.2020.09.033.
15. Karthika, T., Joseph, J., Das, V.R.A., Nair, N., Charulekha, P., Roji, M.D., and Raj, V.S. (2021). SARS-CoV-2 cellular entry is independent of the ACE2 cytoplasmic domain signaling. Cells *10*, 1814. https://doi.org/10.3390/cells10071814.
16. Yan, F.-F., and Gao, F. (2021). Comparison of the binding characteristics of SARS-CoV and SARS-CoV-2 RBDs to ACE2 at different temperatures by MD simulations. Brief. Bioinform. *22*, 1122–1136. https://doi.org/10.1093/bib/bbab044.
17. Liu, S.L., Wang, Z.G., Xie, H.Y., Liu, A.A., Lamb, D.C., and Pang, D.W. (2020). Single-virus tracking: from imaging methodologies to virological applications. Chem. Rev. *120*, 1936–1979. https://doi.org/10.1021/acs.chemrev.9b00692.

18. Heintzmann, R., and Huser, T. (2017). Super-resolution structured illumination microscopy. Chem. Rev. *117*, 13890–13908. https://doi.org/10.1021/acs.chemrev.7b00218.

19. Huang, X., Fan, J., Li, L., Liu, H., Wu, R., Wu, Y., Wei, L., Mao, H., Lal, A., Xi, P., et al. (2018). Fast, long-term, super-resolution imaging with Hessian structured illumination microscopy. Nat. Biotechnol. *36*, 451–459. https://doi.org/10.1038/nbt.4115.

20. Guo, Y., Li, D., Zhang, S., Yang, Y., Liu, J.J., Wang, X., Liu, C., Milkie, D.E., Moore, R.P., Tulu, U.S., et al. (2018). Visualizing intracellular organelle and cytoskeletal interactions at nanoscale resolution on millisecond timescales. Cell *175*, 1430–1442.e17. https://doi.org/10.1016/j.cell.2018.09.057.

21. Han, Y., Li, M., Qiu, F., Zhang, M., and Zhang, Y.-H. (2017). Cell-permeable organic fluorescent probes for live-cell long-term super-resolution imaging reveal lysosome-mitochondrion interactions. Nat. Commun. *8*, 1307. https://doi.org/10.1038/s41467-017-01503-6.

22. Fang, H., Geng, S., Hao, M., Chen, Q., Liu, M., Liu, C., Tian, Z., Wang, C., Takebe, T., Guan, J.-L., et al. (2021). Simultaneous Zn^{2+} tracking in multiple organelles using super-resolution morphology-correlated organelle identification in living cells. Nat. Commun. *12*, 109. https://doi.org/10.1038/s41467-020-20309-7.

23. Chen, J., Wang, C., Liu, W., Qiao, Q., Qi, H., Zhou, W., Xu, N., Li, J., Piao, H., Tan, D., et al. (2021). Stable super-resolution imaging of lipid droplet dynamics through a buffer strategy with a hydrogen-bond sensitive fluorogenic probe. Angew. Chem. Int. Ed. Engl. *60*, 25104–25113. https://doi.org/10.1002/ange.202111052.

24. Chen, J., Liu, W., Fang, X., Qiao, Q., and Xu, Z. (2022). BODIPY 493 acts as a bright buffering fluorogenic probe for super-resolution imaging of lipid droplet dynamics. Chin. Chem. Lett. *33*, 5042–5046. https://doi.org/10.1016/j.cclet.2022.03.120.

25. Wang, L., Frei, M.S., Salim, A., and Johnsson, K. (2019). Small-molecule fluorescent probes for live-cell super-resolution microscopy. J. Am. Chem. Soc. *141*, 2770–2781. https://doi.org/10.1021/jacs.8b11134.

26. Zhou, W., Fang, X., Qiao, Q., Jiang, W., Zhang, Y., and Xu, Z. (2021). Quantitative assessment of rhodamine spectra. Chin. Chem. Lett. *32*, 943–946. https://doi.org/10.1016/j.cclet.2021.02.003.

27. Chi, W., Qiao, Q., Wang, C., Zheng, J., Zhou, W., Xu, N., Wu, X., Jiang, X., Tan, D., Xu, Z., et al. (2020). Descriptor ΔG(C-O) enables the quantitative design of spontaneously blinking rhodamines for live-cell super-resolution imaging. Angew. Chem. Int. Ed. Engl. *59*, 20215–20223. https://doi.org/10.1002/ange.202010169.

28. Qi, Q., Chi, W., Li, Y., Qiao, Q., Chen, J., Miao, L., Zhang, Y., Li, J., Ji, W., Xu, T., et al. (2019). A H-bond strategy to develop acid-resistant photoswitchable rhodamine spirolactams for super-resolution single-molecule localization microscopy. Chem. Sci. *10*, 4914–4922. https://doi.org/10.1039/C9SC01284B.

29. Gautier, A., Juillerat, A., Heinis, C., Corrêa, I.R., Jr., Kindermann, M., Beaufils, F., and Johnsson, K. (2008). An engineered protein tag for multiprotein labeling in living cells. Chem. Biol. *15*, 128–136. https://doi.org/10.1016/j.chembiol.2008.01.007.

30. Los, G.V., Encell, L.P., McDougall, M.G., Hartzell, D.D., Karassina, N., Zimprich, C., Wood, M.G., Learish, R., Ohana, R.F., Urh, M., et al. (2008). HaloTag: a novel protein labeling technology for cell imaging and protein analysis. ACS Chem. Biol. *3*, 373–382. https://doi.org/10.1021/cb800025k.

31. Leng, S., Qiao, Q., Miao, L., Deng, W., Cui, J., and Xu, Z. (2017). A wash-free SNAP-tag fluorogenic probe based on the additive effects of quencher release and environmental sensitivity. Chem. Commun. *53*, 6448–6451. https://doi.org/10.1039/C7CC01483J.

32. Qiao, Q., Liu, W., Chen, J., Zhou, W., Yin, W., Miao, L., Cui, J., and Xu, Z. (2017). A naphthalimide-derived fluorogenic probe for SNAP-tag with a fast record labeling rate. Dyes Pigm. *147*, 327–333. https://doi.org/10.1016/j.dyepig.2017.08.032.

33. Liu, A.A., Zhang, Z., Sun, E.Z., Zheng, Z., Zhang, Z.L., Hu, Q., Wang, H., and Pang, D.W. (2016). Simultaneous visualization of parental and progeny viruses by a capsid-specific HaloTag labeling strategy. ACS Nano *10*, 1147–1155. https://doi.org/10.1021/acsnano.5b06438.

34. Liu, W., Qiao, Q., Zheng, J., Chen, J., Zhou, W., Xu, N., Li, J., Miao, L., and Xu, Z. (2021). An assembly-regulated SNAP-tag fluorogenic probe for long-term super-resolution imaging of mitochondrial dynamics. Biosens. Bioelectron. *176*, 112886. https://doi.org/10.1016/j.bios.2020.112886.

35. Liu, W., Chen, J., Qiao, Q., Liu, X., and Xu, Z. (2022). A TICS-fluorophore based probe for dual-color GSH imaging. Chin. Chem. Lett. *33*, 4943–4947. https://doi.org/10.1016/j.cclet.2022.03.121.

36. Zhang, H., Wada, J., Hida, K., Tsuchiyama, Y., Hiragushi, K., Shikata, K., Wang, H., Lin, S., Kanwar, Y.S., and Makino, H. (2001). Collectrin, a collecting duct-specific transmembrane glycoprotein, is a novel homolog of ACE2 and is developmentally regulated in embryonic kidneys. J. Biol. Chem. *276*, 17132–17139. https://doi.org/10.1074/jbc.M006723200.

37. Kaksonen, M., and Roux, A. (2018). Mechanisms of clathrin-mediated endocytosis. Nat. Rev. Mol. Cell Biol. *19*, 313–326. https://doi.org/10.1038/nrm.2017.132.

38. Lukinavičius, G., Umezawa, K., Olivier, N., Honigmann, A., Yang, G., Plass, T., Mueller, V., Reymond, L., Corrêa, I.R., Jr., Luo, Z.G., et al. (2013). A near-infrared fluorophore for live-cell super-resolution microscopy of cellular proteins. Nat. Chem. *5*, 132–139. https://doi.org/10.1038/nchem.1546.

39. Vickers, C., Hales, P., Kaushik, V., Dick, L., Gavin, J., Tang, J., Godbout, K., Parsons, T., Baronas, E., Hsieh, F., et al. (2002). Hydrolysis of biological peptides by human angiotensin-converting enzyme-related carboxypeptidase. J. Biol. Chem. *277*, 14838–14843. https://doi.org/10.1074/jbc.M200581200.

40. Yang, N., and Shen, H.M. (2020). Targeting the endocytic pathway and autophagy process as a novel therapeutic strategy in COVID-19. Int. J. Biol. Sci. *16*, 1724–1731. https://doi.org/10.7150/ijbs.45498.

41. Rink, J., Ghigo, E., Kalaidzidis, Y., and Zerial, M. (2005). Rab conversion as a mechanism of progression from early to late endosomes. Cell *122*, 735–749. https://doi.org/10.1016/j.cell.2005.06.043.

42. Pelkmans, L., and Helenius, A. (2003). Insider information: what viruses tell us about endocytosis. Curr. Opin. Cell Biol. *15*, 414–422. https://doi.org/10.1016/S0955-0674(03)00081-4.

43. Lazartigues, E., Feng, Y., and Lavoie, J.L. (2007). The two fACEs of the tissue renin-angiotensin systems: implication in cardiovascular diseases. Curr. Pharm. Des. *13*, 1231–1245. https://doi.org/10.2174/138161207780618911.

44. Deshotels, M.R., Xia, H., Sriramula, S., Lazartigues, E., and Filipeanu, C.M. (2014). Angiotensin II mediates angiotensin converting enzyme type 2 internalization and degradation through an angiotensin ii type i receptor–dependent mechanism. Hypertension *64*, 1368–1375. https://doi.org/10.1161/HYPERTENSIONAHA.114.03743.

45. Wang, S., Qiu, Z., Hou, Y., Deng, X., Xu, W., Zheng, T., Wu, P., Xie, S., Bian, W., Zhang, C., et al. (2021). AXL is a candidate receptor for SARS-CoV-2 that promotes infection of pulmonary and bronchial epithelial cells. Cell Res. *31*, 126–140. https://doi.org/10.1038/s41422-020-00460-y.

46. Cantuti-Castelvetri, L., Ojha, R., Pedro, L.D., Djannatian, M., Franz, J., Kuivanen, S., van der Meer, F., Kallio, K., Kaya, T., Anastasina, M., et al. (2020). Neuropilin-1 facilitates SARS-CoV-2 cell entry and infectivity. Science *370*, 856–860. https://doi.org/10.1126/science.abd2985.

47. Yuan, Z., Pavel, M.A., Wang, H., Kwachukwu, J.C., Mediouni, S., Jablonski, J.A., Nettles, K.W., Reddy, C.B., Valente, S.T., and Hansen, S.B. (2022). Hydroxychloroquine blocks SARS-CoV-2 entry into the endocytic pathway in mammalian cell culture. Commun. Biol. *5*, 958. https://doi.org/10.1038/s42003-022-03841-8.

48. Hu, T.Y., Frieman, M., and Wolfram, J. (2020). Insights from nanomedicine into chloriquine efficacy against COVID-19. Nat. Nanotechnol. *15*, 247–249. https://doi.org/10.1038/s41565-020-0674-9.

49. Harada, M., Sakisaka, S., Yoshitake, M., Kin, M., Ohishi, M., Shakado, S., Mimura, Y., Noguchi, K., Sata, M., and Tanikawa, K. (1996). Bafilomycin A1, a specific inhibitor of vacuolar-type H(+)-ATPases, inhibits the

receptor-mediated endocytosis of asialoglycoproteins in isolated rat hepatocytes. J. Hepatol. *24*, 594–603. https://doi.org/10.1016/s0168-8278(96)80146-2.

50. Trivedi, P.C., Bartlett, J.J., and Pulinilkunnil, T. (2020). Lysosomal biology and function: modern view of cellular debris bin. Cells *9*, 1131. https://doi.org/10.3390/cells9051131.
51. Saffi, G.T., and Botelho, R.J. (2019). Lysosome fission: planning for an exit. Trends Cell Biol. *29*, 635–646. https://doi.org/10.1016/j.tcb.2019.05.003.
52. Renard, H.-F., Johannes, L., and Morsomme, P. (2018). Increasing diversity of biological membrane fission mechanisms. Trends Cell Biol. *28*, 274–286. https://doi.org/10.1016/j.tcb.2017.12.001.
53. Bright, N.A., Gratian, M.J., and Luzio, J.P. (2005). Endocytic delivery to lysosomes mediated by concurrent fusion and kissing events in living cells. Curr. Biol. *15*, 360–365. https://doi.org/10.1016/j.cub.2005.01.049.
54. Ghosh, S., Dellibovi-Ragheb, T.A., Kerviel, A., Pak, E., Qiu, Q., Fisher, M., Takvorian, P.M., Bleck, C., Hsu, V.W., Fehr, A.R., et al. (2020). Beta-coronaviruses use lysosomes for egress instead of the biosynthetic secretory pathway. Cell *183*, 1520–1535.e14. https://doi.org/10.1016/j.cell.2020.10.039.
55. Angeli, F., Reboldi, G., and Verdecchia, P. (2021). SARS-CoV-2 infection and ACE2 inhibition. J. Hypertens. *39*, 1555–1558. https://doi.org/10.1097/HJH.0000000000002859.
56. Angeli, F., Zappa, M., Reboldi, G., Trapasso, M., Cavallini, C., Spanevello, A., and Verdecchia, P. (2021). The pivotal link between ACE2 deficiency and SARS-CoV-2 infection: one year later. Eur. J. Intern. Med. *93*, 28–34. https://doi.org/10.1016/j.ejim.2021.09.007.
57. Verdecchia, P., Cavallini, C., Spanevello, A., and Angeli, F. (2020). The pivotal link between ACE2 deficiency and SARS-CoV-2 infection. Eur. J. Intern. Med. *76*, 14–20. https://doi.org/10.1016/j.ejim.2020.04.037.
58. Portales, A.E., Mustafá, E.R., McCarthy, C.I., Cornejo, M.P., Couto, P.M., Gironacci, M.M., Caramelo, J.J., Perelló, M., and Raingo, J. (2022). ACE2 internalization induced by a SARS-CoV-2 recombinant protein is modulated by angiotensin II type 1 and bradykinin 2 receptors. Life Sci. *293*, 120284. https://doi.org/10.1016/j.lfs.2021.120284.
59. Gourdelier, M., Swain, J., Arone, C., Mouttou, A., Bracquemond, D., Merida, P., Saffarian, S., Lyonnais, S., Favard, C., and Muriaux, D. (2022). Optimized production and fluorescent labeling of SARS-CoV-2 virus-like particles. Sci. Rep. *12*, 14651. https://doi.org/10.1038/s41598-022-18681-z.

STAR★METHODS

KEY RESOURCES TABLE

REAGENT or RESOURCE	SOURCE	IDENTIFIER
Antibodies		
SARS-CoV-2 RBD neutralizing antibody rabbit mAb	Sino Biological	Cat # 40592-R001; RRID: AB_2857936
ACE2 Monoclonal antibody Mouse	Proteintech	Cat # 66699-1-Ig; RRID: AB_2882052
SARS-CoV-2 Spike RBD Mouse mAb	ABclonal	Cat # A20141
HRP-conjugated Goat Anti-Mouse IgG(H+L)	Proteintech	Cat # SA00001-1; RRID: AB_2722565
Mouse anti-β-actin mAb	Proteintech	Cat # 66009-1-Ig; RRID: AB_2687938
Rhodamine (TRITC)–conjugated Goat Anti-Mouse IgG(H+L)	Proteintech	Cat # SA00007-1; RRID: AB_2889940
Chemicals, peptides, and recombinant proteins		
Hoechst 33342	ThermoFisher	Cat # 62249
8-well Nunc Lab-Tek	ThermoFisher	Cat # 155411
Lipofectamine 3000	ThermoFisher	Cat # L3000008
Polyethylenimine MAX 40K	Polysciences	Cat # 24765
Expression medium	Sino Biological	Cat # SMM 293-TI
cell culture supplement	Sino Biological	Cat # M293-SUPI
SNAP-Cy3	New England BioLabs	Cat # S9112S
SNAP-Alexa 488	New England BioLabs	Cat # S9129S
Lyso561	KeyGEN BioTECH	Cat # KGMP006
Bafilomycin A1	MedChemExpress	Cat # HY-100558
MCA-APK(Dnp)-OH	Beyotime	Cat # P9737
Dynasore	TargetMOI	Cat # T1848
HCQ	Sigma-Aldrich	Cat # H0915
CQ	Innochem	Cat # A88133
Experimental models: Cell lines		
Hela cells	ATCC	Cat #CCL-2
HEK293T	ATCC	Cat #CRL3216
NCI-H1299	ATCC	Cat # CRL-5803
Vero	ATCC	Cat #CCL-81
Caco-2	ATCC	Cat #HTB-37
Expi293F™ Cells	ThermoFisher	Cat #A14527
Recombinant DNA		
mCherry-Rab7A	Rowland et al. 2014	Addgene plasmid # 61804
EGFP-Rab5A Q79L	Sun et al. 2010	Addgene plasmid # 28046
EYFP-actin	a gift from Professor Tao Xu (Institute of Biophysics, Chinese Academy of Sciences)	N/A
LAMP1-mCherry	a gift from Professor Tao Xu (Institute of Biophysics, Chinese Academy of Sciences)	N/A
Spike-T-mGam	a gift from Professor Tong Cheng (Xiamen University)	N/A
pcDNA3.1-h-RBD	This paper	N/A
pcDNA3.1-s-ACE2	This paper	N/A
Software and algorithms		
Image J	Schneider et al., 2012	RRID: SCR_003070 https://imagej.nih.gov/ij/download.html

(*Continued on next page*)

Continued

REAGENT or RESOURCE	SOURCE	IDENTIFIER
Other		
Fluorescence spectrophotometer	Agilent	N/A
Laser Scanning Confocal Microscope	Andor	iQ 3.2
N-SIM Super-Resolution Microscope System	Nikon	N/A

RESOURCE AVAILABILITY

Lead contact

Further information and requests for resources and reagents should be directed to and will be fulfilled by the lead contact, Zhaochao Xu (zcxu@dicp.ac.cn).

Materials availability

Plasmids generated in this study are available upon request and materials transfer agreement (MTA).

Data and code availability

- The authors declare that all data supporting the findings of this study are available within the paper and its supplemental information files.
- This paper does not report original code.
- Additional Supplemental Items are available from Mendeley Data: https://doi.org/10.17632/xzb2kr344j.1. And any other additional information required to reanalyze the data reported in this paper is available from the lead contact upon request.

EXPERIMENTAL MODEL AND SUBJECT DETAILS

Cell lines

NCI-H1299 cells (CRL-5803, human, male) were grown in RPMI medium, whereas the other cell lines (Hela cells: CCL-2, human, female; HEK293T: CRL3216, human, sex unknown; Vero: CCL-81, monkey, sex unknown; Caco-2: HTB-37, human, male) were grown in DMEM. All cell media were supplemented with 10% fetal bovine serum and 1% streptomycin-penicillin, at 37°C (5% CO_2). Cell lines were checked regularly for any mycoplasma contamination.

METHOD DETAILS

Fusion protein expression and purification

The synthetic RBD-Halo (Halo tag was fused to the C-terminal of the receptor binding domain (RBD) of wild-type SARS-CoV-2 spike) or SNAP-ACE2 (SNAP tag was fused to the C-terminal of the full-length gene of human angiotensin-converting enzyme 2 (ACE2)) cDNA gene sequence was cloned into pcDNA3.1 vector to obtain pcDNA3.1-h-RBD and pcDNA3.1-s-ACE2 expression vector. For the expression of h-RBD or Spike-T-mGam protein, the pcDNA3.1-h-RBD or Spike-T-mGam vector was transiently transfected to 293-F cells (Thermo Fisher, human, sex unknown) with polyethylenimine, and the cells were cultured with serum-free expression medium (SMM 293-TI). On the 1st, 3rd and 5th day after transfection, serum-free cell culture supplement was added to the culture solution. After culturing for 7 days, h-RBD fusion protein was purified from filtered cell supernatants using Ni-NTA resin (GE Healthcare).

Probe synthesis

Compound NHS-TMSiR (5 mg, 8.77 μmol) and HaloTag amine (4 mg, 17.54 μmol) were dissolved in 1 mL dry DMF and the solution was stirred overnight at room temperature. The solvent was removed under reduce pressure and the residue was further purified by silica gel chromatography (PE/EA = 50:1-10:1; V/V) to afforded Halo-SiR (5 mg, 84%) as a colorless solid. ^{1}H NMR (400 MHz, $CDCl_3$) δ 7.99 (d, *J* = 8.0 Hz, 1H), 7.91 (d, *J* = 8.0 Hz, 1H), 7.67 (s, 1H), 6.97 (s, 2H), 6.79 (d, *J* = 8.9 Hz, 2H), 6.71 (s, 1H), 6.57 (d, *J* = 8.6 Hz, 2H), 3.76 – 3.58 (m, 6H), 3.55 (d, *J* = 4.3 Hz, 2H), 3.50 (t, *J* = 6.6 Hz, 2H), 3.39 (t, *J* = 6.6 Hz, 2H), 2.97 (s, 12H), 1.75 – 1.69 (m, 2H), 1.56 – 1.48 (m, 2H), 1.40 (dd, *J* = 15.3, 7.5 Hz, 2H), 1.30 (m, *J* = 6.9 Hz, 2H), 0.63 (s, *J* = 29.1 Hz, 6H). HRMS (ESI) m/z found 678.3144 $[M+H]^+$, calculated 677.3051 for $C_{37}H_{48}ClN_3O_5Si$

^{1}H-NMR spectra were recorded on a Bruker 400 spectrometer with TMS as an internal standard. Chemical shifts were given in ppm and coupling constants (*J*) in Hz. High-resolution mass spectrometry (HRMS) data were obtained with an LC/Q-TOF MS spectrometer. HRMS spectrum of Halo-SiR was shown as follow.

SDS-PAGE/Western Blot analysis

The fusion protein h-RBD was reacted with 3-fold molar concentration of probe Halo-SiR in PBS buffer (20mM, pH = 7.4) at 37°C for 2 h, obtaining h-RBD-SiR. The h-RBD and h-RBD-SiR were then mixed with loading buffer (1% SDS, 10% glycerol, 10 mM Tris-HCL PH 6.8, 1mM EDTA, DTT (dithiolthreitor) and pinch of bromophenole blue) and boiled for 5 min, respectively. Protein solution and protein marker were loaded into 15% Sodium dodecyl sulfate polyacrylamide gel electrophoresis (SDS-PAGE) gel. The run was carried out at 100 volt in 1xTris/glycine SDS-running buffer. After electrophoresis, the gel was first photographed in a dark room under UV-light. Then, it was stained with Coomassie Brilliant Blue and photographed. Then, the Western Blot (WB) process was carried out.

For the western blotting assay quantifying RBD and ACE2 proteins, HEK293T cells were collected and washed with 1x PBS before lysed with RIPA buffer (Seven Biotech) with PMSF protease inhibitor in presence. The cell lysis process lasted 5 minutes, and cells lysates were collected to centrifuge for 10 min at 12,000 g, and protein concentration was determined with the Coomassie Brilliant Blue. For the WB of h-RBD protein, 50 nM RBD protein with or without 50 μM dynasore were incubated to s-ACE2 overexpressed HEK 293T cells. WB was performed from both cell lysates and supernatants after 2h or 20h incubation. For the WB of s-ACE2 protein, the HEK293T cells were treated with or without 100 nM MCA-APK-OH, 50 nM h-RBD, and 50 μM dynasore. After incubation for 20 h, cell lysates were collected for WB. Samples were run on pre-made SDS-PAGE gels and then the gels were transferred onto PVDF membranes (Yeasen) along with Rapid Trans-Blot 1X Buffer (Seven Biotech, SW171-02) and run in a Trans-Blot Turbo system for 2 h at 200 mA. Immunoblots were blocked with 5% skim milk dissolved in 1x TBS with 1% Tween-20 (TBST) at RT time for 2 h. And then they incubated overnight at 4°C separately with the following primary antibodies: the mouse anti-ACE2 mAb (1:6000), mouse anti-RBD mAb (1: 4000), and mouse anti-β-actin mAb (1: 40000). After three vigorous washes of TBST, the mouse anti-goat HRP conjugated secondary mAb (1: 60000) was incubated to the membranes at 4°C for 2 h. they were then exposed through an ECL luminescence kit. All the strips were quantified by the ImagJ software.

Live-cell imaging of RBD-ACE2 interaction

Hela cells (ATCC CCL-2) were seeded into 8-well Nunc Lab-Tek confocal imaging plate with 70−80% confluency. The cells were then transfected with 125 ng pcDNA3.1-s-ACE2 vector per well using Lipofectamine 3000. 24 h later, the cells were incubated with the fresh medium containing 500 nM SNAP-Cy3, 25 nM h-RBD-SiR, and 1 μM Hoechst 33342. After incubation for 1 h at 37°C in the presence of 5% CO_2, the fluorescence imaging was performed with 100 × oil-dripping objective lens by using ANDOR™ living cell laser scanning confocal microscope. For SNAP-Cy3, λ_{ex} = 561 nm, λ_{em} = 580-650 nm; For Halo-SiR, λ_{ex} = 640 nm, λ_{em} = 660-700 nm.

Live-cell tracking of h-RBD internalization

Hela and HEK293T cells seeded in 8-well confocal imaging plates were transfected with 125 ng pcDNA3.1-s-ACE2 vector. After transfection for 24 h, the first group cells were treated with 250 nM SNAP-Alexa 488 only, the second group cells were treated with 250 nM SNAP-Alexa 488 and 25 nM h-RBD-SiR, and the third group cells were pretreated with 50 μM dynasore for 30 min, then incubated with 250 nM SNAP-Alexa 488 and 25 nM h-RBD-SiR. The fluorescence imaging was acquired every 10 min between 20 and 100 min. The imaging was performed with 100 × oil-dripping objective lens by using ANDOR™ living cell laser scanning confocal microscope. For s-ACE2-488, λ_{ex} = 488 nm, λ_{em} = 500-550 nm; For h-RBD-SiR, λ_{ex} = 640 nm, λ_{em} = 660-700 nm.

Live-cell evaluation of inhibitors

To evaluate the RBD neutralization properties of inhibitors, the inhibitor was pre-incubated with h-RBD-SiR for 30 min. and then cells were treated with SNAP-Alexa 488 and pre-incubated solution for 1 h. The fluorescence imaging was acquired with 10 × objective lens. The calculation of relative binding activity of h-RBD to s-ACE2 is as described in quantification and statistical analysis.

For the evaluation of inhibiting effect on RBD endocytosis, the Hela/s-ACE2 cells were pretreated with or without (control group) inhibitors for 30 min in optimum culture conditions, and then 250 nM SNAP-Alexa 488 and 25 nM h-RBD-SiR were added. The imaging was performed every 30 min with 100 × oil-dripping objective lens. Experiments were done in triplicate and 5 cells of each test were tracked.

The inhibitors used in this paper were 40 nM RBD neutralizing antibody, 50 μM dynasore, 50 μM hydroxychloroquine, 50 μM chloroquine, 20 mM NH_4Cl, and 100 nM Bafilomycin A.

SIM dynamics imaging: transport and maturation of h-RBD&s-ACE2 vesicles

s-ACE2&h-RBD vesicular maturation

EGFP-Rab5A was acquired by mutating the residue Leu79 of EGFP-Rab5A Q79L to Gln with one-step site-directed mutation method (primers of F:TGGTCAAGAACGATACCATAGC, R:TATCGTTCTTGACCAGCTGTATC). Hela cells were transiently co-transfected with pcDNA3.1-s-ACE2&EGFP-Rab5A or pcDNA3.1-s-ACE2&mCherry-Rab57A using Lipofectamine 3000. After 24 h culturing, the cells were treated with 250 nM SNAP-Cy3 and 25 nM h-RBD-SiR. After incubation for 1h and 6h, respectively, the fluorescence imaging was performed with N-SIM Super-Resolution Microscope. Colocalization were quantified using the Pearson colocalization coefficient application in ImageJ.

Dynamics imaging of Rab7A or actin on h-RBD&s-ACE2 vesicles

We co-transfected pcDNA3.1-s-ACE2 and mCherry-Rab7A/EYFP-actin to Hela cells. After culturing for 24 h, the cells were treated with 250 nM SNAP-Alexa488 and 25 nM h-RBD-SiR. After 1h incubation, a long-term dynamic tracking of the cells was carried out. The time interval between each SIM image was 1 min with a course of 35 min.

The transport of s-ACE2&h-RBD vesicles

In order to monitor the movement of h-RBD&s-ACE2 internalization vesicles along tubulin, we co-transfected pcDNA3.1-s-ACE2 and mCherry-Tubulin to Hela cells and cultured for 24 h. The cells were then treated with 250 nM SNAP-Alexa488 and 25 nM h-RBD-SiR. After 1h incubation, long-term cellular dynamic tracking was carried out by N-SIM in three optical channels. The time interval between each SIM image was 1 min with a course of 33 min.

For Rab5-EGFP, EYFP-actin and SNAP-Alexa488, λ_{ex} = 488 nm, λ_{em} = 500-550 nm; For SNAP-Cy3, mCherry-Rab7, and mCherry-Tubulin: λ_{ex} = 561 nm, λ_{em} = 580-650 nm; For Halo-SiR, λ_{ex} = 640 nm, λ_{em} = 660-700 nm.

SIM imaging to resolve the destinations of both h-RBD and s-ACE2

Hela cells were transiently transfected with pcDNA3.1-s-ACE2 and cultured for 24h. The cells were treated with 250 nM SNAP-Alexa488 for 30 min. After washing for two times, a fresh medium containing 25 nM h-RBD-SiR was added to the cells. The cells were cultured at 37°C in the presence of 5% CO_2. The SIM imaging was carried out after 2h, 10h, and 16h culturing of the cells, respectively. Before imaging, 1 μM Lys561 was added to the medium and incubated for 10 min.

Hela cells were co-transfected with pcDNA3.1-s-ACE2 and LAMP1-mCherry and cultured for 24h. The cells were pre-incubated with 250 nM SNAP-Alexa488 (for drug group, both 250 nM SNAP-Alexa488 and 100 nM Bafilomycin A) for 30 min. After washing for two times, the cell culture medium was replaced with a fresh medium containing 25 nM h-RBD-SiR (for drug group, both 25 nM h-RBD-SiR and 100 nM Bafilomycin A). The SIM imaging was carried out after 16h culturing of the cells at 37°C in the presence of 5% CO_2

QUANTIFICATION AND STATISTICAL ANALYSIS

For the evaluation of h-RBD and s-ACE2 activity in living cells, the s-ACE2-expressed Hela cells were treated with 500 nM SNAP-Cy3 and different concentrations of h-RBD-SiR (600 nM, 400 nM, 200 nM, 100 nM, 50 nM, 25 nM, 6.25 nM, and 1.56 nM), respectively. The fluorescence imaging was performed with 10 × objective lens. The mean fluorescence intensity of random 20 cells at 561nm and 640 nm channels (IF_{640}^{cells},IF_{561}^{cells}), as well as randomly delineated background fluorescences (IF_{640}^{bg},IF_{561}^{bg}), was collected. The relative binding activity (RBA) of h-RBD to s-ACE2 was calculated according to this formula: $RBA = \frac{IF_{640}^{cells} - IF_{640}^{bg}}{IF_{561}^{cells} - IF_{561}^{bg}}$. These experiments were repeated three times.

Statistical analyses were performed in Prism 8 (Graphpad) or Microsoft Excel. The error bars in the figures refer to mean plus standard deviation (SD) values. For RBD internalization in Figure 2, the statistical analysis was by one-way ANOVA (ns: $p > 0.5$, *: $p < 0.5$, **: $p < 0.05$, ***: $p < 0.005$, ****: $p < 0.0005$). For pearson's correlation coefficient in Figures 3 and 4, the statistical analysis used two-tailed t tests and P values were considered significant when $p < 0.01$ and denoted as *$p < 1$, **$p < 0.1$, ****$p < 0.001$.